Keio University

1858

CALAMVS GLADIO FORTIOR

Annual Report on Research Activities 2017

(Volume 7)

Tanabe Photonic Structure Group,

Department of Electronics and Electrical Engineering,

Faculty of Science and Technology, Keio University

Contents

Foreword

Thank you very much for your continued support and interest in the research and educational activities at the Tanabe Photonic Nanostructure Laboratory, the Department of Electronic Engineering, in Keio University.

This year, we are focusing on the development of optical frequency comb light sources using microresonators, which require the fusion of micro- and nano-photonics, and ultrafast optics. It is often not easy to cover all of the broad area in one group. Therefore, we are seeking domestic and international collaborations. With this in mind, I particularly encouraged the students to actively participate in international conferences and learn cutting-edge researches by themselves. As a result of this, we presented three papers in CLEO, five in CLEO/Europe that was held in Germany, two papers in CLEO/Pacific-rim held in Singapore, and five papers in FiO/LS held in Washington DC. I am proud that we were able to support 14 students to participate in those international conferences this year. I think it is important for the students to learn the cutting-edge research and even have opportunities to directly interacting with those researchers, who usually see their names only in textbooks and papers. I believe that diversity is becoming increasingly important for the maturity of the laboratory culture. In that respect, it was a very meaningful year.

In this report, we will report on some of the research we conducted in FY2017. I would like to note that the manuscripts were written by my students with minimal editing; so if you have trouble with the language and contents, please do not hesitate to contact me. Although some of the papers might have some issue with the language, I would like to stress that I am confident that the research is of high impact and contains originality that will benefit the research community. If you are interested in our research, please contact us; we are always open for collaboration. Thank you very much for your interest.

December 2018

Takasumi Tanabe, Associate Professor,
Department of Electronics and Electrical Engineering,
Keio University

Lab Members (Names and their positions after graduation)

Associate Professor: Takasumi Tanabe

Secretary:

Naoko Kojima	(until July 2017)
Kaoru Onodera	(from July 2017)

Post-doctor:

Tsutaru Kumagai	Research Fellowship for Young Scientist, JSPS (PD)

PhD Students:

Tomohiro Tetsumoto	PhD in Engineering, Graduates the graduate school of Keio University
Nurul Ashikin Binti Daud	Continues in the graduate school of Keio University
Ryo Suzuki	Continues in the graduate school of Keio University Leading Graduate School RA (global environment system leader) Research Fellowship for Young Scientist, JSPS (DC1)

Master 2nd Grade: (The class of 2015)

Naoya Hirota	Graduates the graduate school of Keio University
Shun Fujii	Continues his PhD in the graduate school of Keio University
Atsuhiro Hori	Graduates the graduate school of Keio University

Master 1st Grade: (The class of 2016)

Takumi Okamura	Continues in the graduate school of Keio University
Naotaka Kamioka	Continues in the graduate school of Keio University
Akihiro Kubota	Continues in the graduate school of Keio University
Mika Fuchida	Continues in the graduate school of Keio University
Yoshihiro Honda	Continues in the graduate school of Keio University

Bachelor 4th Grade: (The class of 2017)

Rammaru Ishida	Continues in the graduate school of Keio University
Shengi Jin	Continues in the graduate school of Keio University
Minoru Hasegawa	Will graduate Keio University in (Sep. 2018)

Research Activities

High *Q* TE & TM modes in a silica nanobeam cavity

Tomohiro Tetsumoto (D3)

We fabricated a nanobeam type one-dimensional photonic crystal (PhC) nanocavity made of silica, and measured its optical properties. Two orthogonal modes of the transverse electric (TE) mode and the transverse magnetic (TM) mode, were observed with *Q* values exceeding ten thousand, which are the highest reported values for silica PhC nanocavities. We also investigated the optimum coupling condition between a cavity and a nanofiber, and obtained a high coupling efficiency (CE) of 87% with an optical mode with a *Q* of over ten thousand.

Key words: Photonic crystal nanocavity; Silica; Polarization diversity; Optical nanofiber;

1. Background

PhC nanocavities have various applications including in quantum optics and optical signal processing since they efficiently enhance light-matter interactions [1, 2]. However, most of them are fabricated in-plane owing to their ease of fabrication, and have poor spatial symmetry three-dimensionally. Thus it is difficult to obtain resonant modes with in-plane and out-of-plane polarization in the same wavelength range. On the other hand, the use of a variety of polarizations has recently been investigated in some research fields. For example, the circular polarization dependence of states with spin-orbit coupling and valley states has been studied in the field of cavity quantum electrodynamics [3]. In this study, we design, fabricate, and evaluate a PhC nanocavity with in-plane and out-of-plane polarizations of the TE and TM modes in a one-dimensional PhC configuration

2. Design & Fabrication

A cavity was formed by arranging periodic air holes in a silica beam structure, and reducing the distance between the holes (lattice constant) gradually toward the center of the cavity. Figure 1(a) and (b) show the transmission spectra and mode profiles of a cavity calculated with the finite difference time domain (FDTD) method. The fundamental and second-order modes of the TE and TM modes were obtained in the same wavelength range. Figure 2(a) shows the cavity fabrication procedure. To set the cavity resonant wavelength in the telecom range, it was necessary to employ a silica device layer with a thickness of 800 nm, which made it difficult to obtain a sufficient selection ratio with an organic resist. Therefore, we employed a silicon mask with a higher selection ratio with the silica device layer for etching. First, we formed a silicon mask layer and a silica mask layer on the silica device layer by using sputtering and chemical vapor deposition, respectively. Then, we applied a resist to the silica mask layer and drew mask patterns with electron beam lithography. Next, we etched the silica mask layer, the silicon mask layer, and the silica device layer sequentially using anisotropic dry etching. After that, we etched a silicon sacrificial layer isotopically with XeF_2 gas and realized an air-bridge structure. Figure 2(b) and (c) show the fabricated fine structures.

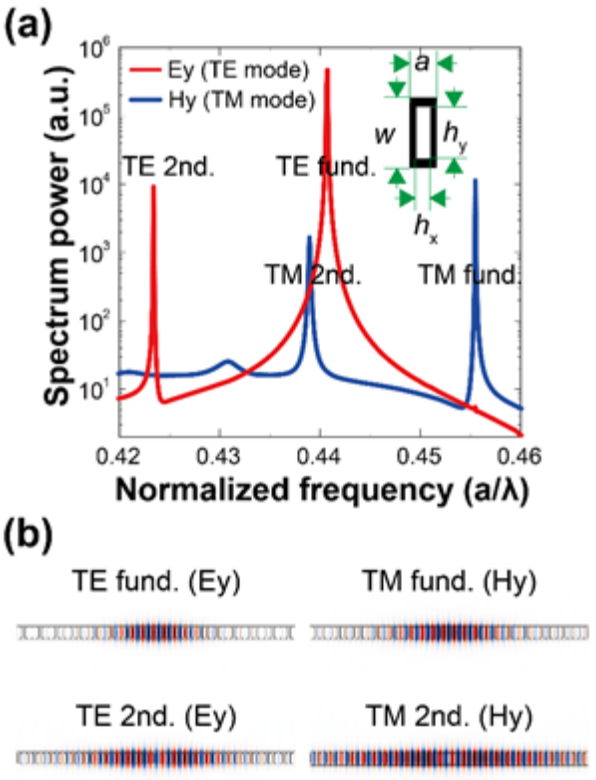

Fig. 1: (a) Resonant spectra of the cavity calculated with the FDTD method. The inset shows a unit cell of the cavity. Lattice constant $a = 770$ nm, width $w = 2.6a$, thickness $t = 1.1a$, hole depth $h_x = 0.5a$, hole width $h_y = 0.7w$. (b) Cavity mode profiles calculated with the FDTD method.

3. Optical measurement

Optical measurement was demonstrated in a side coupling configuration with an optical nanofiber.

Figure 3(a) shows the obtained transmission spectra. We observed the fundamental and second-order modes of the TE and TM modes as predicted by the FDTD calculation in Fig. 1(a). The orthogonality of the two modes was confirmed as shown in the inset of Fig. 3(a). The highest Qs were $Q_{TE} = 2.4\times10^4$ for the TE mode and $Q_{TM} = 1.0\times10^4$ for the TM mode, which are the highest reported values for silica PhC nanocavities.

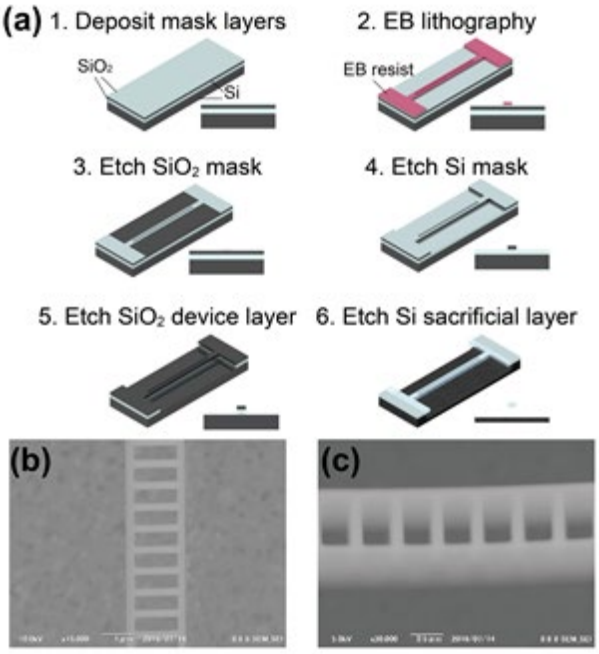

Fig. 2: (a) Cavity fabrication procedure. (b) Fabricated structures.

We also investigated the change in the CE when we reduced the gap between the cavity and the nanofiber by moving the sample stage upward (inset of Fig. 4). Note that the loss components of Q are expressed by the following equations.

$$Q_{\mathrm{load}}^{-1} = Q_{\mathrm{int}}^{-1} + Q_{\mathrm{coup}}^{-1} \quad (1)$$

$$Tr = \left(\frac{1}{1 + Q_{\mathrm{int}}/Q_{\mathrm{coup}}}\right)^2 \quad (2)$$

Q_{load}, Q_{int}, Q_{coup}, and Tr are the loaded Q, intrinsic Q, coupling Q, and transmittance respectively. CE has the relation CE = 1 - Tr. Figure 4 shows the obtained Q dependence versus the gap distance for the TE and TM modes. The intrinsic Q is required to be sufficiently larger than the coupling Q to achieve a high CE (low Tr) as described by Eq. (2). The condition will generally be satisfied when the gap is small, and only the coupling Q is decreased, however, a decrease in the intrinsic Q was observed simultaneously when the stage displacement increased. This was due to the influence of the effective index of the cavity caused by the presence of nanofiber near the cavity structure. We found this trade-off relation in the experiment, and obtained a high CE of 87% with an optical mode with a Q of over 10^4 by properly adjusting the gap distance.

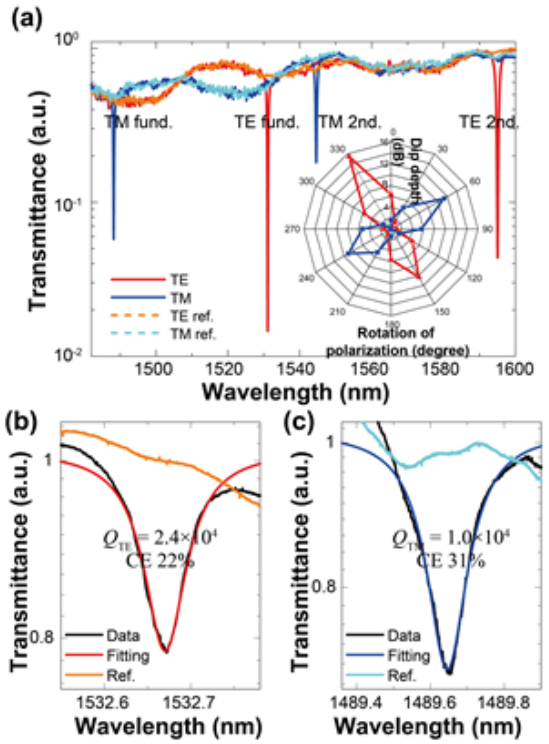

Fig. 3: (a) Measured transmission spectrum. The inset shows the CE dependence versus the input light polarization for TE and TM fundamental modes. The highest obtained Qs of (b) TE and (c) TM modes.

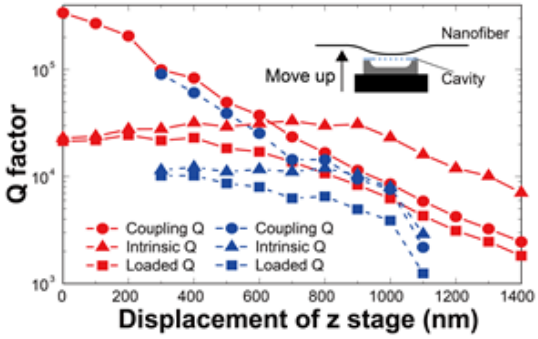

Fig. 4: Q dependence versus the gap between the cavity and a nanofiber. The inset shows a schematic of the positional relationship of the cavity and the nanofiber.

4. Conclusion

We designed, fabricated, and measured a silica nanobeam cavity with TE and TM modes in the same wavelength range. The cavity exhibited Qs of over 10^4, which are the highest reported values for silica PhC nanocavities. We also realized a proper coupling condition between the cavity and an optical nanofiber, and achieved a high CE of 87% with a mode with a Q value of over 10^4. This study described a design strategy for PhC nanocavities suitable for applications that require polarization

diversity, and showed that achieving a high Q is possible with the cavities.

Acknowledgements

The cavity was fabricated using facilities at the National Institute of Information and Communications Technology. We thank Dr. Sekine and Dr. Furusawa for their cooperation with the fabrication and the administration staff for allowing me to use the facilities.

References

[1] S. Noda, M. Fujita, and T. Asano, Nature Photon. **1**, 449–458 (2007).
[2] T. Tanabe, M. Notomi, H. Taniyama, and E. Kuramochi, Phys. Rev. Lett. **102**, 043907 (2009).
[3] D. Xiao, *et al.*, Phys. Rev. Lett. **108**, 196802 (2012).

Improved CMOS compatible photonic crystal demultiplexer

Shengji Jin (B4)

We optimized a compact photolithographically fabricated photonic crystal DeMUX and obtained flat and high transmittance between channels. A thermal analysis showed that a footprint of 110 μm²/ch is possible with PhC technology.

Key words: Wavelength filtering devices, Photolithography, Photonic crystals

1. Introduction

Wavelength division multiplexing (WDM) technologies are used in long-haul optical communications, but new technologies such as IoT and big data are increasing the data rate required for all distances. Thus, WDM is starting to be used even for short-range communications such as in a data center or between server racks. It is not hard to believe that this trend will continue in the future, and WDM technologies may be required even for on-board or in-chip data transmittance. To support this approaching era, we need devices that are extremely low cost and compact, with moderate performance (compared with devices used in long-haul communications; i.e. a smaller number of supported channels etc.). A demultiplexer (DeMUX) is one of the devices employed in WDM systems, where it is used to divide an input signal into different channels. An arrayed waveguide grating is often used for longer distances [1][2], and silicon photonic devices are now expected to support optical systems used in data centers. However, for even shorter distances, we need to develop technologies that have a smaller footprint and lower cost.

Photonic crystal (PhC) is an attractive candidate [3], which can confine light in a very small space. We have already fabricated a PhC DeMUX with CMOS compatible photolithography [4], because the CMOS process will enable future mass production. The PhC DeMUX is much smaller than an AWG DeMUX and is silica clad, which makes it environmentally stable and robust. However, there were still certain problems, including a large transmittance loss (−32.7 dB), a large transmittance variance between channels (−16.2 dB), and a large crosstalk (−8.36 dB).

In this study, we optimized our structure and attempted to realize high and equal transmittance in each channel, and a low crosstalk. In addition, we studied the minimum possible footprint by performing a heat simulation and revealing the distance needed to avoid heat interference between channels.

2. Design and optical property of optimized PhC DeMUX

Figure 1(a) shows a SEM image of the fabricated DeMUX. A bus waveguide is coupled with eight PhC nanocavities with different resonances, which will drop the resonant light towards the output port. A TiN heater is integrated at the top of each PhC nanocavity to control the resonance of the cavities. It has a footprint of 43.7 μm². Figure 1(b) shows the DeMUX filter in detail, where the lattice constant is changed at intervals of 1 nm (from 420 nm to 413 nm) to [enable/provide?] eight different resonances.

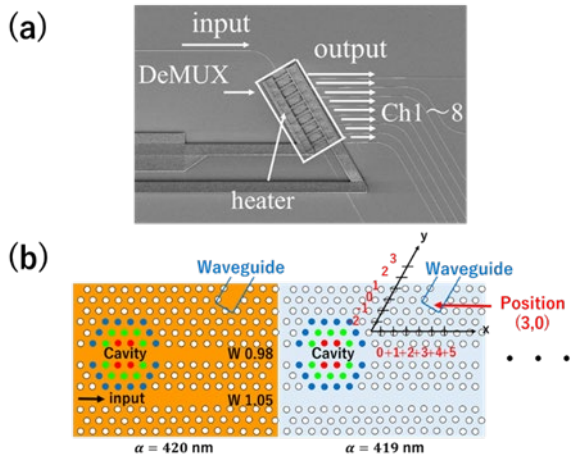

Fig. 1. (a) SEM image of fabricated DeMUX. (b) Schematic illustration of the nanocavities used for the PhC DeMUX. It shows the optimization strategy regarding the position of the output waveguide.

To optimize the crosstalk and the transmittance, we changed the position of the output waveguide. Figure 1(b) shows how we defined the position of the output waveguide[, for example/using?] (x, y). We calculated the transmittance at different x and y values, and found that (3, 0) provided the best performance.

Following the calculation, we fabricated the structure at position (3, 0) and measured the transmittance. Figure 2(a) and 2(b) show the transmittance spectra before (0, 0) and after (3, 0) the optimization, respectively.

At position (0,0), the device exhibited a fiber-to-fiber insertion loss of −32.7 dB, which improved to −17.9 dB. The fluctuation between the peaks of the eight channels was −16.2 dB, and the crosstalk was −8.36 dB at position (0, 0). These values improved to −5.5 dB and −29.3 dB at position (3, 0).

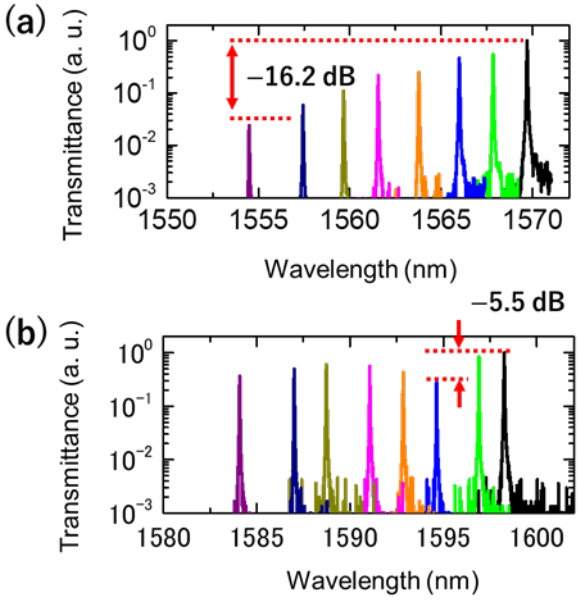

Fig. 2. Measured normalized transmittance spectrum for (0,0) structure (a); and for (3, 0) structure (b).

We optimized the optical property and showed that our compact PhC DeMUX is sufficient to support applications that require compactness and low cost with moderate transmittance characteristics.

3. Numerical analysis of thermal interference of small PhC DeMUX

However, we still face a challenge, namely the realization of equidistant channel spacing. This problem may be caused by fabrication error. With the (3, 0) structure, the average channel spacing is 240 GHz, where the standard deviation is 57.6 GHz.

To adjust the resonance, we need to use heaters, which may lead to thermal interference with different channels when we place the cavities too close to each other. Thus, the thermal property is one of the limiting factors determining the minimum size of this DeMUX.

We calculated the heat transfer using the model shown in Fig. 3(a). A heater equipped with an 8.8×10^{13} W/m^3 heat source is placed 1.2 μm above the nanocavity. When we set the *x*-axis (at the center of a 210-nm thick silicon slab) as shown in Fig. 3(a), the temperature at each point is shown in Fig. 3(b), when the heater at Ch. 2 is activated.

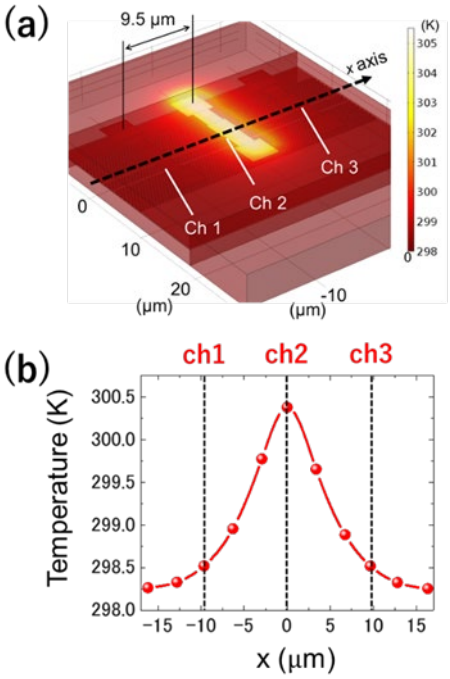

Fig. 3. (a) Structure and calculated temperature distribution of a DeMUX with a channel spacing of 9.5 μm. (b) Calculated temperature along the *x*-axis.

The temperature increases 2.4 K, which corresponds to a ~90 GHz shift in the resonance frequency. On the other hand, the temperature increases 0.52 K at the position of ch. 1, which is sufficiently small to avoid thermal interference. We may move ch. 1 slightly closer to ch. 2, but the spacing appears almost optimum. Thus, the footprint of 110 μm^2/ch might be the smallest possible for a PhC DeMUX. It should be noted that a footprint of 110 μm^2/ch is needed for a silicon microresonator DeMUX, which shows the advantage of a PhC device over conventional silicon photonic devices.

4. Summary

We designed and fabricated a CMOS compatible PhC DeMUX with an optimized structure and obtained significant improvements, namely high transmittance, channel flatness, and low crosstalk. We also analyzed the thermal property of this structure and obtained the minimum possible channel spacing without encountering the problem of thermal interference. As a result, we should be able to obtain a small footprint of 110 μm^2/ch, and thus outperform other reported devices.

References

[1] S. Cheung, *et al.*, J. Sel. Top. Quantum Electron. **20**, 8202207 (2014).
[2] Q. Fang, *et al.*, Opt. Express **18**, 5106 (2010).
[3] Y. Takahashi, *et al.*, Opt. Express **22**, 4692 (2014).
[4] Y. Ooka, *et al.*, Opt. Express **25**, 1521 (2017).

Light emission from MoS_2 on various substrates for application to photonic nanostructures

Rammaru Ishida (B4) Tomohiro Tetsumoto (D3)

MoS_2 is attracting intense research interest because it evolves into a direct bandgap semiconductor only when an MoS_2 crystal is reduced to monolayer thickness. We studied monolayer fabrication and identified the number of layers exactly using Raman spectra. The measured photoluminescence (PL) intensity for a monolayer was about 30 times stronger than that for a bilayer. In addition, we transferred MoS_2 to various substrates, and evaluated the optical property from the PL intensity. The PL intensity on graphene was enhanced more than 10-fold compared with the intensity at a fiber tip. Our study indicates that a graphene substrate is a satisfactory candidate for MoS_2 application.

Key words: 2D materials; molybdenum disulfide; monolayer exfoliation; PL enhancement

1. Introduction

It is well-known that graphite-like 2D materials can be exfoliated by using a Scotch tape method [1]. More than 60 different types of 2D materials have been investigated with this method, and MoS_2 is one that has been garnering intense research interest because of its outstanding optical properties. As the number of layers is reduced from bulk to monolayer, this 2D material evolves from an indirect to a direct bandgap semiconductor [2]. This interesting material property is used in many fields including light-emitting devices [3], and photodetectors [4].

A problem is that the quantum efficiency of MoS_2 is not high. This is mainly due to [the/its?] thickness of under 1 nm and the small light emission region. It remains a great challenge to enhance the quantum efficiency and thus enable MoS_2 to be applied to light emitting devices. A number of laboratories have engaged energetically in enhancing the quantum efficiency by such means as exploiting the strong Purcell effect in a photonic crystal, and fabricating quantum dots in a monolayer. In terms of the Purcell effect, spontaneous emission is enhanced by the Purcell factor F in Eq. (1).

$$F = \frac{3Q\lambda_c}{4\pi^2 V} \quad (1)$$

This equation indicates that a cavity with a high Q and a small mode volume V is required for quantum efficiency enhancement. For this reason, monolayer MoS_2 is often integrated with nanocavities. However, since the state of the substrate surface can have a negative effect on the optical property of MoS_2, the enhancement can be quenched.

In this research, we study how to fabricate and transfer monolayer MoS_2, and then we collect photoluminescence (PL) spectra from monolayers on different substrates.

2. Fabrication of monolayer and measurement of optical properties

Nitto N-380 tape and Gel-Pak PF film ×4 were used to fabricate the monolayer. The way to exfoliate a monolayer is shown in Fig. 1. First, bulk MoS_2 (SPI Supplies) is placed on Nitto tape and covered with a second piece of the same tape. Then we mechanically cleave the crystal by pulling the tapes apart. This process is repeated about 10 times. After that, the tape is attached to a 5-mm-square piece of polydimethylsiloxane (PDMS). Finally, after cleaving at an appropriate speed, a monolayer is fabricated on the PDMS. The fabricated structure is shown in Fig. 2(a). The monolayer is indicated with a white arrow.

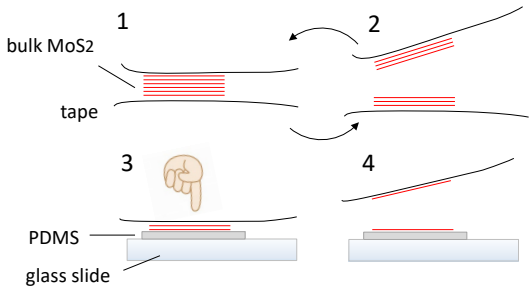

Fig. 1: Monolayer fabrication process

Raman spectroscopy is used to identify the number of layers. As shown in Fig. 2(b), the left peak is attributed to the in-plane vibration of MoS_2 and the right peak results from out-of-plane vibration. Previous research demonstrated that there is a relationship between the Raman spectrum and the number of layers. The left peak undergoes a red shift while the right peak undergoes a blue shift as the number of layers decreases [5]. This is mainly due to the decrease in the van der Waals force along the c-axis of the

material. Fig. 2(b) shows that the number of layers is identified, and this agrees well with previous research.

The measured PL intensity for a monolayer and

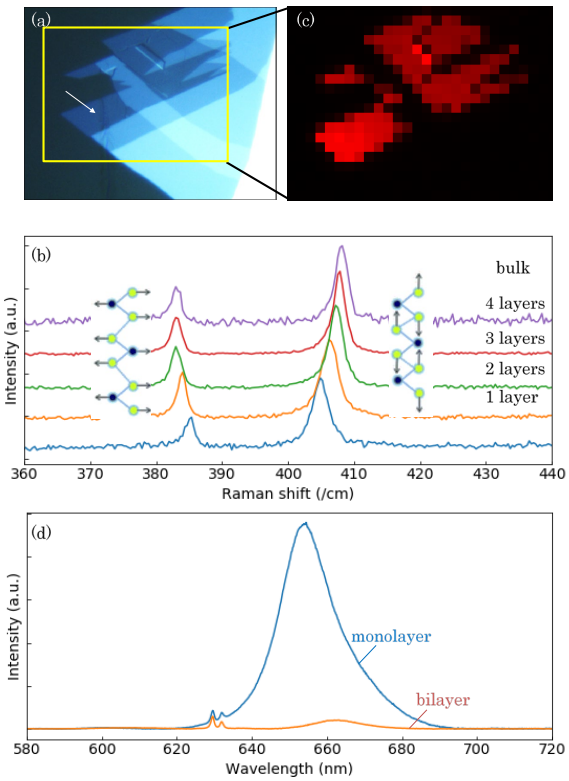

Fig. 2: (a) Fabricated structure. The monolayer is indicated by a white arrow. (b) Raman spectra of bulk and few-layer MoS_2. (c) PL Mapping of MoS_2. (d) PL spectra for monolayer and bilayer MoS_2

a bilayer differ greatly as shown in Fig. 2(d). As mentioned above, the former are direct bandgap semiconductors and the latter are indirect bandgap semiconductors. This figure indicates that the PL peak is about 660 nm and the intensity increases about 30-fold when the MoS_2 crystal is thinned to a monolayer. We also mapped the PL intensity inside the yellow frame in Fig. 2(c) with the PL at 660 nm. It is clear from Fig. 2(c) that only the monolayer becomes bright.

3. Transfer monolayer to fiber tip and compare PL for various substrates

We described how to fabricate a monolayer on PDMS. Here, we introduce how to transfer a monolayer to a fiber tip shown in Fig. 3(a).

The monolayer can be transferred by attaching the fiber to the monolayer and then detaching it very slowly. Since the adhesive force of the PDMS is lower than the van der Waals force between the monolayer and the fiber, the monolayer is attached to the fiber tip. The monolayer shown in Fig. 2(a) is transferred as shown in Fig. 3(b). It is clear that the monolayer can be transferred without breaking the structure.

To clarify the influence of the substrate on PL

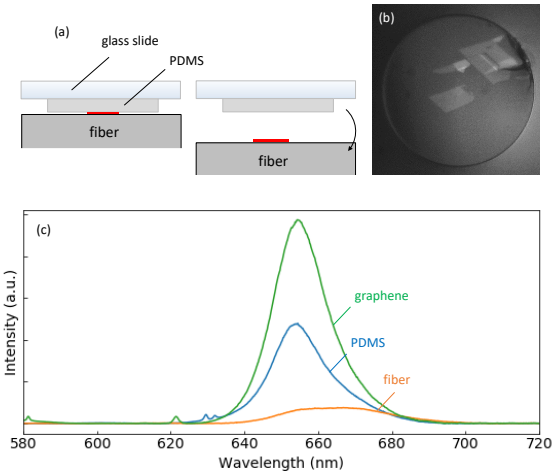

Fig. 3: (a) Monolayer transfer process. (b) Image of transferred monolayer on fiber tip. (c) PL spectra of monolayer MoS_2 on 10-layer graphene, PDMS and fiber.

intensity, we transferred a monolayer to 10-layer graphene and a fiber tip. Fig. 3(c) shows the PL intensity on these substrates, and reveals that the PL intensity on graphene is more than 10 times stronger than that on the fiber tip. The increased PL intensity is mainly attributed to the dangling bond on the substrate surface and the surface roughness. In terms of the dangling bond, previous research has indicated theoretically that an O-dangling bond at the SiO_2 surface modifies the electronic properties of the MoS_2 and causes a transition from a direct to an indirect bandgap semiconductor [6]. Since 2D materials have no dangling bond, it is appropriate to use graphene as a substrate so that the optical property of MoS_2 can be fully utilized.

4. Conclusion

We studied how to fabricate and transfer monolayer MoS_2. The number of layers was exactly identified from changes in PL intensity and Raman spectra. We also evaluated the substrate according to the PL intensity of the monolayer. It is important to use 2D materials as the substrate because they have no dangling bonds

References

[1] K. S. Novoselov, et al., Science **306**, 666-669 (2004)
[2] Kin Fai Mak, et al., Phys. Rev. Lett **105**, 136805 (2010)
[3] Chul-Ho Lee, et al., Nat. Nanotech. **9**, 676–681 (2014)
[4] Xudong Wang, et al., Adv. Mat. **27**, 6575 (2015)
[5] Changgu Lee, et al., ACS Nano **4(5)**, 2695-2700 (2010)
[6] Ha-Jun Sung, Duk-Hyun Choe and K J Chang, New Journal of Physics **16** , 113055 (2014)

Saturable absorption by carbon nanotubes on silica microtoroids

Tsutaru Kumagai (PD) Naoya Hirota (M2)

Saturable absorption is a key technology for shaping light waveforms as, for example, in passive mode-locking. The combination of high-Q optical microcavities with a saturable absorber allows stable lasing and soliton formation. This work describes saturable absorption by carbon nanotubes (CNTs) on silica microtoroids. The CNTs were grown on silica microtoroids by chemical vapor deposition (CVD). Raman spectroscopy revealed that the CNTs were of good quality (G/D ratio ~7) and about 1.0 nm in diameter, thus confirming that a sample can be prepared for use in the telecommunication band. A counter-propagating pump-probe experiment enabled us to investigate the characteristics of CNTs as saturable absorbers while suppressing thermo-optic bistability in a microcavity system. The results revealed a saturable absorption coefficient of 0.042 cm^{-1}, a saturable intensity of 25.9 MW/cm^2, and a modulation depth of 28%.

Key words: Silica microtoroid cavity, carbon nanotubes (CNTs), saturable absorption, chemical vapor deposition (CVD).

1. Introduction

A high-Q microcavity [1] can confine light in a small space, and thus enable a strong interaction between light and matter. Various optical nonlinearities, such as stimulated Raman scattering and cascaded four-wave mixing, are observed at a low input power in a microcavity [2]. Since these effects allow us to obtain multimode lasing, it is of great interest to develop a small pulsed laser source by achieving phase locking between different transverse modes. Indeed, studies of a broadband optical frequency comb, known as a Raman comb or Kerr comb, have been reported that employed whispering-gallery mode (WGM) microcavities [3-6]. Frequency comb generation at various wavelengths is of particular interest thanks to its potential sensing and spectroscopy applications.

Although mode locking has been demonstrated in a microcavity with a Kerr comb, it requires precise control of the cavity dispersion and other parameters such as the wavelength tuning and power adjustment of the input laser. Therefore, mode locking is rarely easy or straightforward, especially when we target different wavelength regimes or use a different nonlinearity such as stimulated Raman scattering [5,6]. In such cases, the use of a saturable absorber would allow us to achieve mode locking as has been demonstrated with rare-earth-doped fiber ring lasers.

Nano-carbon materials such as single-walled and semiconductor type carbon nanotubes (CNTs) and graphene have been suggested as new saturable absorbers [7]. These materials are both inexpensive and space-saving. Moreover, they exhibit a broad absorption band in the telecommunication wavelength regime, high power stability [8], and a short recovery time [9], which are advantageous characteristics with a view to practical use. In particular, the CNT bandgap can be controlled by controlling its diameter and chirality. Various types of saturable absorbers that use CNTs have been demonstrated in fiber lasers and solid-state lasers. Evanescent field interaction types such as D-shaped fiber and tapered fiber are particularly suitable for the devices because of their excellent stability and reliability [10].

Here, we study the saturable absorption behavior of CNTs on a silica microtoroid for stable mode locking. We use chemical vapor deposition (CVD) to allow selective growth because the CNTs are synthesized on a catalyst [11]. The combination of CVD and electron beam (EB) lithography allows us to control the grown CNTs in terms of position and amount. We employ a counter-propagating pump-probe experiment to measure the saturable absorption, where we accurately characterize the detuning of the pump from the resonance of the hot cavity that is needed to obtain the pump power. We investigate the characteristics of CNTs as saturable absorbers.

2. Device fabrication and characterization

After the fabrication of the silica toroids, EB lithography and alcohol catalytic CVD were employed to selectively grow CNTs on the microcavity surface [12-14]. First, oxygen plasma was employed to clean the surfaces of the toroids. A resist was spin coated on the silica toroids, and then densified at 180°C for 3 min. A line was then

patterned by EB lithography and developed by using a xylene solution. A 1-Å layer of cobalt catalyst was deposited on the substrate by evaporation, and then the resist was removed with dichloromethane and acetone solutions. Single-walled CNTs were grown on the patterned cobalt catalyst by the CVD method with ethanol under an Ar-H_2 gas flow at 870°C.

Figure 1 shows the spatial mapping of the Raman intensity and Raman spectrum, where the peak intensity of the G-band is used for the mapping. The irradiation point of the laser is shown with a white circle. The Raman spectrum shows clear G and D bands. The G band is the vibration mode of graphene, and the D band originates from defects. Hence, the G/D ratio provides an index reflecting the quality of the CNTs. Since this value is 7, we consider the CNTs to have been well prepared. The wavenumber of the radial breathing mode (RBM) is dependent on the diameter of CNTs as follows [15],

$$d = \frac{K}{\omega_{\mathrm{RBM}}} \qquad (1)$$

where $K = 248$ (in cm^{-1}·nm), and ω_{RBM} is the peak wavenumber of the RBM. The ω_{RBM} values are 146.8, 171.0, 182.3, and 229.2 cm^{-1}; therefore, the calculated diameters are 1.69, 1.45, 1.36, and 1.08 nm, respectively. Thus, the CNT bandgaps are 0.50, 0.57, 0.68, and 0.78 eV, based on calculation data obtained for electronic transition energies versus nanotube diameters. From these results, we prepared a device that operates in the telecommunication band (~0.8 eV = 1550 nm).

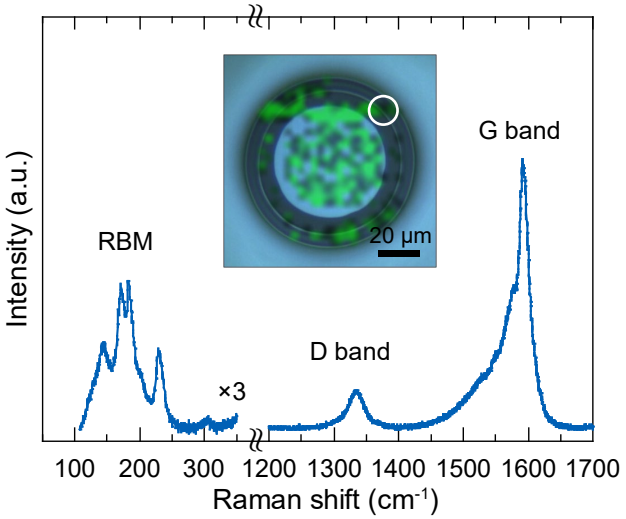

Fig. 1: Observation of silica microtoroid with Raman spectroscope. The mapping image is obtained by using the intensity of the G band of the Raman spectrum. RBM: radial breathing mode. The G band is the vibration mode of graphene, and the D band originates from defects.

3. Optical measurement

Figure 2(a) shows the experimental setup. We designed a counter-propagating pump-probe setup, where a weak continuous-wave probe is injected from the opposite side of the setup where its frequency is scanned to measure the cavity transmittance spectrum. This will allow us to measure the transmittance spectrum of a hot cavity without it exhibiting spectrum modulation based on thermo-optic bistability.

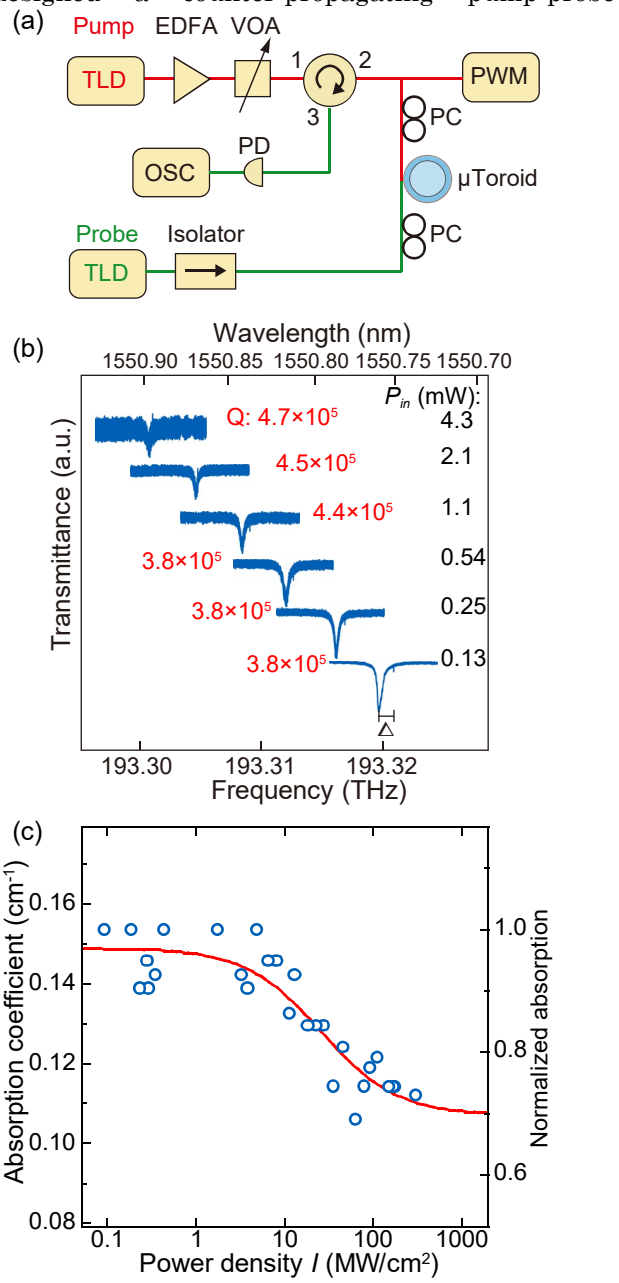

Fig. 2(a) Setup for the counter-propagating pump-probe experiment. (b) Transmittance spectra of the probe light recorded with OSC. (c) Absorption coefficient as a function of power density I of the coupled light in a microtoroid. The blue circles are data. The red line is a fitted curve.

Figure 2(b) is the measured result for the device shown in Fig. 1. It shows the transmission spectrum of the probe light for different input powers P_{in} and detunings Δ of the pump. We observe a small dip on the higher frequency side of

the resonant mode, which is caused by interference between the backscattered pump and probe lights; thus, we can directly measure Δ with our counter-propagating pump-probe setup. When the pump light is off, Q is 4.0×10^5 with a resonant frequency at 193.319 THz. When P_{in} increases, the resonant frequency of the cavity shifts towards the lower frequency side as a result of the thermo-optic effect. At the same time, the width of the resonance decreases as the input power increases, that is, the Q value is increased. The measured Q values are shown in Fig. 2(b). Since a high Q is achieved with a low loss, the result indicates that the loss is smaller at a higher pump power, which is a strong indication of saturable absorption behavior.

Figure 2(c) shows the plot of the absorption coefficient as a function of power density I. Now it is clear that the absorption coefficient is smaller at a higher power density, because of the saturable absorption. The absorption coefficient of the saturable absorber is given as [16],

$$\alpha(I) = \frac{\alpha_{SA}}{1 + I/I_{sat}} + \alpha_{NS} \qquad (2)$$

where α_{SA} is the saturable absorption coefficient, α_{NS} is the non-saturable absorption coefficient, and I_{sat} is the saturable intensity, which is the intensity when the value of α_{SA} is halved. Using least square fitting, we obtained α_{SA} = 0.042 cm^{-1}, α_{NS} = 0.107 cm^{-1}, and I_{sat} = 25.9 MW/cm^2, where the fitted curve is shown by the red line in Fig. 2(c). The modulation depth is defined as $\alpha_{SA}/(\alpha_{SA}+\alpha_{NS})$, and is 28%. The saturable absorption behavior from the CNTs on the silica microtoroid is demonstrated with the counter-propagating pump-probe experiment.

4. Conclusion

We demonstrated saturable absorption by CNTs on silica microtoroids. Good quality CNTs (G/D ratio ~ 7) with a diameter of about 1.0 nm were fabricated on silica microtoroids by CVD. The CNT growth with CVD is suitable for the fabrication of such devices because the CNTs can be prepared while controlling various parameters such as number and position. A counter-propagating pump-probe experiment enabled us to investigate the characteristics of CNTs as saturable absorbers, because it could measure the transmittance spectrum of a microcavity with a strong pump without exhibiting thermo-optic bistability. We measured a saturable absorption coefficient, saturable intensity, and modulation depth of 0.042 cm^{-1}, 25.9 MW/cm^2, and 28%, respectively. This is the first demonstration of saturable absorption in silica microtoroids, and this concept may offer the possibility of obtaining robust mode-locked frequency combs.

Acknowledgements

This work was supported by JSPS KAKENHI (#JP15H05429 and #JP16J10230) and a Grant-in-Aid for JSPS Fellows, and also by PRESTO (JPMJPR152B) from JST.

The authors thank Mr. Katsuya Sato, Mr. Koki Namiki, and Prof. Hideyuki Maki at the Maki Laboratory for sample preparation and helpful discussions.

References

[1] K. J. Vahala, Nature, 424, 839 (2003).
[2] I. H. Agha, Y. Okawachi, M. A. Foster, J. E. Sharping and A. L. Gaeta, Physical Review A, 76, 043837 (2007).
[3] T. J. Kippenberg, R. Holzwarth and S. A. Diddams, Science, 332, 555 (2011).
[4] P. Del'Haye, A. Schliesser, O. Arcizet, T. Wilken, R. Holzwarth and T. J. Kippenberg, Nature, 450, 1214 (2007).
[5] W. Liang, V. S. Ilchenko, A. A. Savchenkov, A. B. Matsko, D. Seidel and L. Maleki, Phys. Rev. Lett., 105, 143903 (2010).
[6] G. Lin and Y. K. Chembo, Optics Letters, 41, 3718 (2016).
[7] S. Y. Set, H. Yaguchi, Y. Tanaka and M. Jablonski, Journal of Lightwave Technology, 22, 51 (2004).
[8] Y. W. Song, S. Yamashita and S. Maruyama, Appl. Phys. Lett., 92, 021115 (2008).
[9] J. Wang, Y. Chen and W. J. Blau, J. Mater. Chem., 19, 7425 (2009).
[10] K. Kashiwagi and S. Yamashita, Opt. Express, 17, 18364 (2009).
[11] Y. Murakami, S. Chiashi, Y. Miyauchi, M. Hu, M. Ogura, T. Okubo and S. Maruyama, Chemical Physics Letters, 385, 298 (2004).
[12] K. Masuda, S. Moriyama, Y. Morita, K. Komatsu, T. Takagi, T. Hashimoto, N. Miki, T. Tanabe and H. Maki, Appl. Phys. Lett., 108, 222601 (2016).
[13] T. Mori, Y. Yamauchi, S. Honda and H. Maki, Nano Letters, 14, 3277 (2014).
[14] N. Hibino, S. Suzuki, H. Wakahara, Y. Kobayashi, T. Sato and H. Maki, ACS Nano, 5, 1215 (2011).
[15] A. Jorio, R. Saito, J. H. Hafner, C. M. Lieber, M. Hunter, T. McClure, G. Dresselhaus and M. S. Dresselhaus, Phys. Rev. Lett., 86, 1118 (2001).
[16] F. Wang, A. G. Rozhin, V. Scardaci, Z. Sun, F. Hennrich, I. H. White, W. I. Milne and A. C. Ferrari, Nature Nanotechnol., 3, 738 (2008).

Raman comb formation in a silica microresonator

Ryo Suzuki (D3)

A high-Q microresonator, owing to its short cavity length, can generate light that has a comb-like spectrum (microcomb) in a frequency domain with large mode spacings. In this research, we used a silica microresonator to generate a microcomb via stimulated Raman scattering, and studied the parameter dependence of the comb spectral shape.

Key words: Microresonator, microcomb, stimulated Raman scattering

1. Introduction

A microresonator can confine light on a long time scale and in a small volume, and the intracavity power is increased by inputting a continuous-wave (CW) light. The high intracavity power causes four-wave mixing (FWM), which is an optical nonlinear process. FWM generates light with a comb-like spectrum in the frequency domain (Kerr comb), which corresponds to the microresonator resonance frequency. Kerr combs have a large mode spacing ranging from 10 GHz to a few THz, which is compatible with applications such as optical communication, microwave oscillators, dual-comb spectroscopy, and optical frequency comb sources for astronomy [1]. In addition, microcomb generation via stimulated Raman scattering (SRS) has been reported [2,3].

SRS is an optical nonlinear process that can generate red-shifted light from pump light via an interaction between light and molecular vibrations [4]. Since the wavelength shift is determined by the vibration mode frequency of the host material, each material has a different Raman gain spectrum. Although SRS can provide lasing action and optical amplification, it usually requires very high intensity pumping. Optical microresonators with a high quality factor (Q) and a small mode volume enable us to demonstrate low threshold lasing with CW pumping [5]. Also, multi-mode Raman lasing (Raman comb) can be generated by exciting multiple resonance modes via broadband Raman gain.

Kerr combs broaden the bandwidth via FWM while satisfying the phase matching condition. Hence, each frequency component can be phase-locked. On the other hand, since Raman combs broaden without requiring a phase matching condition, they are not typically phase-locked. However, some research groups have reported phase-locked Raman comb generation whose condition depends on the microresonator dispersion [4,5]. Phase-locked Raman combs are compatible with applications such as compact pulse laser sources, microwave oscillators, sensors, and coherence tomography. However, Raman comb formation has not been understood and methods for controlling the spectral shape have yet to be developed. In this research, we studied the dynamics of Raman comb formation in silica rod microresonators, which have a broadband Raman gain [6].

2. Experiment

A CW laser light with a 100 kHz linewidth was amplified and then coupled to a silica rod microresonator by using a tapered fiber. The coupling strength was adjusted by changing the fiber position. Silica rod microresonators

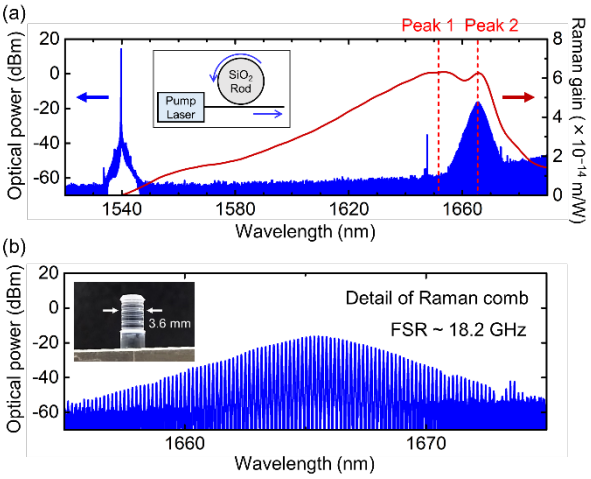

Fig. 1: (a) Optical spectra (blue) and the theoretical Raman gain pumped at 1540 nm (red). The Raman gain has two large peaks with frequency shifts of 13.2 THz (Peak 1) and 14.7 THz (Peak 2). (b) Detail of the generated Raman comb.

with an intrinsic Q (Qi) of over 100 million were fabricated using CO_2 laser processes. We used a microresonator with a diameter of 3.6 mm, which corresponds to a cavity FSR of 18.2 GHz. Figure 1 shows the Raman comb spectra obtained when pumping the resonance mode at 1540 nm with 160 mW. By controlling the pump frequency and coupling strength with the waveguide, we generated a Raman comb with a smooth spectral envelope. The red line in Fig. 1(a) shows the theoretical Raman gain pumped at 1540 nm, which has two peaks (Peaks 1 and 2). In this experiment, we observed the transition of the Raman comb generation between these two peaks.

Figure 2 shows spectrum formation via SRS when changing the detuning and coupling strength. The detuning represents the frequency difference between pump and resonance frequencies. In Fig. 2(a), a pump light with a large amount of detuning generated SRS close to the Peak 1 wavelength. This is because Peak 1 has a larger Raman gain than Peak 2, and this induces the Raman lasing at Peak 1 first. Then, decreasing the detuning induced SRS in a longer wavelength regime, whose offset from the pump matched Peak 2. By further decreasing the detuning, we observed an energy transfer from Peak 1 to Peak 2 and the suppression of the Raman light at Peak 1. This transition occurred by inducing Raman scattering again from shorter wavelength components. Next, we controlled the coupling strength by

changing the tapered fiber position and measured the comb spectra with near zero pump detuning (Fig. 2(b)). The Raman comb, which is shown at top in Fig. 2(b), was generated with the optimal coupling

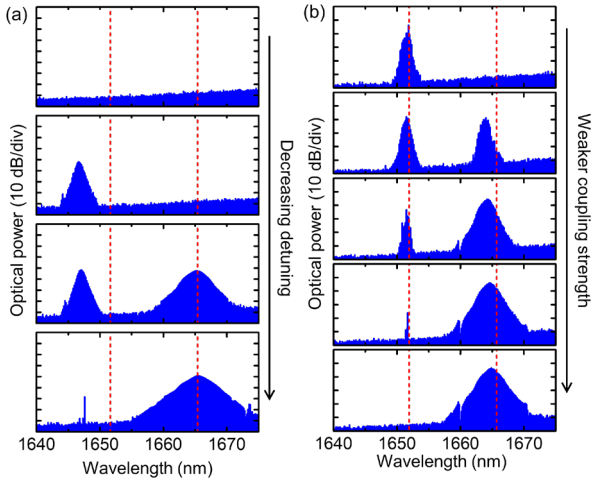

Fig. 2: Raman comb formation when (a) decreasing the detuning between pump and resonance frequencies and (b) reducing the coupling strength. Clear center wavelength transitions were observed in both cases.

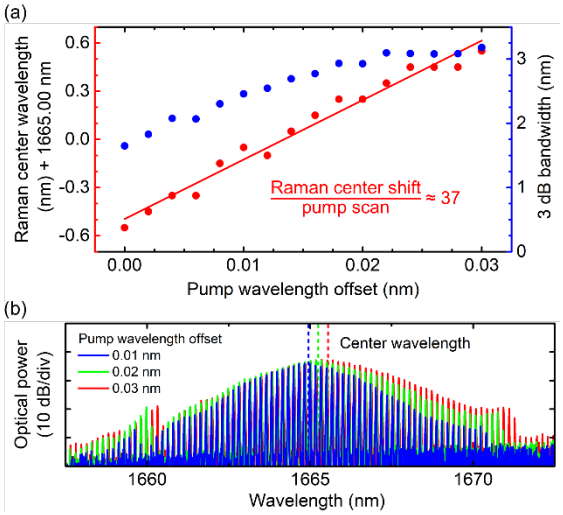

Fig. 3: (a) Center frequency, bandwidth, and (b) spectrum of a Raman comb when changing the pump wavelength.

strength as used in many microresonator studies. However, in this research, weaker coupling can efficiently induce SRS. This is because weak coupling maintains the high Q for resonance modes with a Raman comb, which induces efficient SRS. In conclusion, SRS can be generated efficiently with a small amount of detuning and a low coupling strength leading to the generation of a Raman comb first at Peak 1 and then at Peak 2.

Longer wavelength modes are excited from modes at shorter wavelengths, and this induces the center wavelength of a Raman comb to shift via SRS. Figure 3(a) shows the center wavelength (red) and 3 dB bandwidth (blue) of a Raman comb as a function of the pump wavelength. The center wavelength shift was much larger than with pump scanning, whose ratio is about 37. Figure 4(b) shows Raman comb spectra with different pump wavelengths, which indicate that the comb envelope broadens to a longer wavelength. The center wavelength shift of a mode-locked soliton pulse (corresponding to the pulse delay in the time domain) has been observed in optical fibers and microresonators.

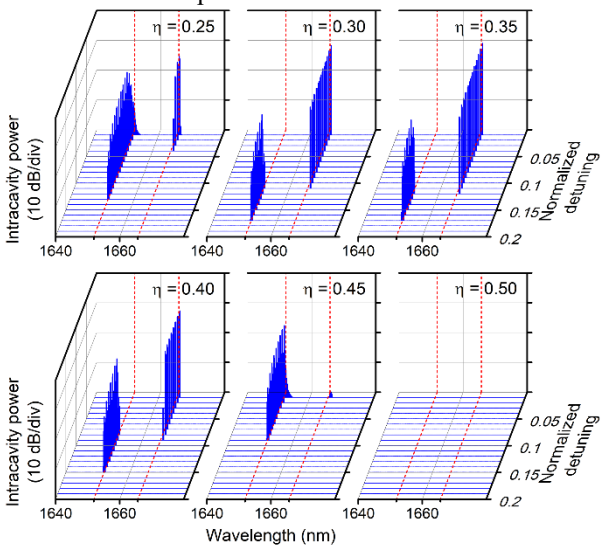

Fig. 4: Calculation results for coupled mode equations, which show that the wavelength SRS depends on the coupling strength and detuning. Red lines show the wavelengths of Peaks 1 and 2.

3. Calculation

To study the energy exchange between the pump and other resonant modes covered by Raman gain, we calculated the numbers of intracavity photons by using coupled mode equations taking Raman processes into account. Figure 4 shows the calculation results, which are in agreement with the experimental observations. The Raman transition from Peak 1 to Peak 2 is reproduced using these equations. The details can be found in Ref. [6].

4. Summary

In summary, we studied the dynamics of Raman comb formation in silica rod microresonators, which have a broadband Raman gain. SRS was generated efficiently with a small amount of detuning and a low coupling strength, which induced the generation of a Raman comb first at Peak 1 and then at Peak 2.

References

[1] V. Brasch, M. Geiselmann, T. Herr, G. Lihachev, M. H. P. Pfeiffer, M. L. Gorodetsky, and T. J. Kippenberg, Science 351, 357-360 (2016).

[2] W. Liang, V. S. Ilchenko, A. A. Savchenkov, A. B. Matsko, D. Seidel, and L. Maleki, Phys. Rev. Lett. 105, 143903 (2010).

[3] G. Lin and Y. K. Chembo, Opt. Lett. 41, 3718–3721 (2016).

[4] G. P. Agrawal, Nonlinear fiber optics (Academic, 2007).

[5] S. M. Spillane, T. J. Kippenberg, and K. J. Vahala, Nature 415, 621-623 (2002).

[6] R. Suzuki, A. Kubota, A. Hori, S. Fujii, and T. Tanabe, J. Opt. Soc. Am. B (accepted).

Numerical simulation of mode coupling assisted dark soliton formation in coupled cavity system

Shun Fujii (M2)

We numerically investigated the generation of a Kerr comb in a normal dispersion microcavity system where mode coupling between two different cavity modes was present. We studied the phase-matching condition theoretically, which helped us to discover suitable parameters for FSR-selectable comb formation. This modeling approach will be a powerful tool for assisting future work as regards dispersion engineering for Kerr comb generation and frequency tuning for deterministic mode-locked comb generation.

Key word: Microresonator, Microcomb, Dark soliton, Nonlinear coupled mode equations

1. Introduction

Kerr frequency comb generation is demonstrated using high-Q microcavities. Kerr combs have been attracting considerable attention because they have various applications thanks to their compactness, low power consumption, and high repetition rate [1]. Although normal dispersion has been considered unsuitable for Kerr comb generation, due to the lack of modulation instability, this problem has been solved by utilizing a mode coupling induced resonance frequency shift. It makes it possible to realize anomalous local dispersion despite the overall dispersion being normal. As a result, modulation instability (MI) occurs in a coupled mode cavity system, and initial sidebands can be generated. This Kerr comb generation process leads to the formation of a dark pulse, and this has been confirmed both experimentally and theoretically [2-3]. These previous studies have ensured that normal dispersion Kerr comb generation is attractive in terms of the efficiency and repeatability of soliton formation.

The Kerr comb formation model has been developed using two approaches: a nonlinear coupled mode equation (NCME) and a Lugiato-Lefever equation (LLE) [4]. Both approaches can well describe comb formation in a microcavity with anomalous group velocity dispersion (GVD). Meanwhile, in the normal GVD regime, exact modeling has remained a challenge due to mode coupling between two different mode families, which is essential for comb generation.

We modeled and simulated mode coupling assisted normal dispersion Kerr comb generation in a coupled cavity system, by using nonlinear coupled mode equations (NCMEs). This modeling (i.e. comb evolution including two different mode families) enabled us not only to simulate in a more rigorous way, but also to find suitable parameters for practical experiments.

2. Model

The Main cavity is coupled to an external waveguide and it is also coupled to an Auxiliary (Aux.) cavity. The coupling rate (in angular frequency) between the Main and Aux. cavity modes is κ. We denote the field amplitude of the Main and Aux. cavity modes with a and b. The loaded decay rates (in angular frequency) of the two cavities (a and b) are γ and γ', where the coupling rate with the external waveguide is also taken into account for γ. The Aux. cavity is used to cause mode coupling with the Main cavity.

Figure 1 shows a diagram of the spectra of the Main and Aux. cavities when two cavities are coupled at mode $\mu = -1$, where μ is the relative longitudinal mode number. ω_μ and ω'_μ are the angular resonant frequencies of the longitudinal modes at mode number μ for the Main and Aux. cavities, respectively. The mode coupling induces two new supermode resonances with frequencies as denoted with $\omega_\mu^{(+)}$ and $\omega_\mu^{(-)}$, where $\omega_\mu^{(+)}$ is the symmetric mode and $\omega_\mu^{(-)}$ is the asymmetric mode. It should be noted that the free-spectral range (FSR) is not equidistant when the cavity system has dispersion, which means that the resonance asymmetry factor Δ_{as} is positive ($\Delta_{as} > 0$) for anomalous dispersion and negative ($\Delta_{as} < 0$) for normal dispersion, when it is defined as $\Delta_{as} = (\omega_\mu - \omega_0) - (\omega_0 - \omega_{-\mu})$. The resonance frequency of the Main cavity is given as $\omega_\mu = \omega_0 + \mu D_1 + (1/2)\mu^2 D_2$, where D_1 is the cavity-FSR, and D_2 is the second-order dispersion. The resonance frequency of the Aux. cavity is shifted by $\Delta\omega$ from the Main cavity, such as $\omega'_\mu = (\omega_0 + \Delta\omega) + \mu D_1 + (1/2)\mu^2 D_2$. When the offset frequency $\Delta\omega$ is zero, the center frequency is equal to that of the main mode, which means that the center modes ($\mu = 0$) of Main and Aux. are strongly coupled. On the other hand, when the offset frequency has a nonzero value, the location at which the strong interaction occurs is changed.

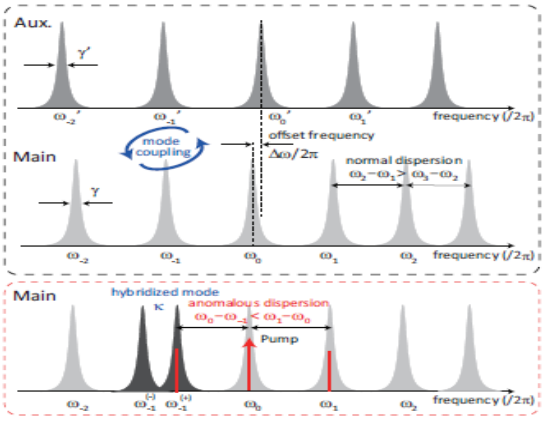

Fig. 1: Schematic diagram of the spectra obtained when two cavities are coupled at mode $\mu = -1$. The pump light is at $\mu = 0$. A hybridized mode is formed at mode $\mu = -1$.

$$\frac{\partial a_\mu}{\partial t} = -\left[\frac{\gamma}{2} + i(\omega_\mu - \omega_p - \mu D_1)\right] a_\mu + ig \sum_{j,k} a_j a_k a^*_{j+k-\mu} + i\frac{\kappa}{2} b_\mu + f\delta_{\mu 0} \quad (1)$$

$$\frac{\partial b_\mu}{\partial t} = -\left[\frac{\gamma'}{2} + i(\omega'_\mu - \omega_p - \mu D'_1)\right] a_\mu + ig' \sum_{j,k} b_j b_k b^*_{j+k-\mu} + i\frac{\kappa}{2} a_\mu \quad (2)$$

Eqs. (1) and (2) are nonlinear coupled mode equations considering two modes A and B , where a_μ (Main) and b_μ (Aux.), respectively, are the slowly varying amplitudes of the two comb mode. ω_p is the frequency of the pump light, and $g=\hbar\omega_0^2 n_2 D_1/(2\pi n_0 A_{eff})$ is the Kerr nonlinear coefficient at the Main cavity, where n_2, n_0, and A_{eff} are the nonlinear refractive index, refractive index, and the effective mode area, respectively. The Kerr nonlinear coefficient g' at the Aux. cavity is defined in a similar way. $f = [\gamma_{ext} P_{in}/(\hbar\omega_p)]^{(1/2)}$ is the external pumping term, and δ_0 is the Kronecker delta indicting that only μ=0 is pumped. The terms on the right-hand side in Eq. (1) represent loss, cavity detuning and dispersion, the Kerr effect, mode couplings, and the external pump. In the following simulation, we calculated a total of 201 modes using the 4th-order Runge-Kutta method and a fast Fourier transform acceleration algorithm.

3. Simulation results

We investigated the phase-matching condition required to initialize sideband generation. Figure 2 shows the asymmetry factor Δ_{as} at different μ values, as a function of $\Delta\omega$. κ is fixed at a constant value ($\kappa/2\pi$ =3.34 GHz). To obtain MI gain we need to satisfy the anomalous dispersion condition ($\Delta_{as} > 0$), whose area is shown in white in Fig. 2. The gray shaded region indicates that there is no MI gain because of the normal dispersion of the system. For instance, when $\Delta\omega$ is tuned in such a way that the mode coupling occurs at $\mu = -3$, the initial sidebands start to appear 3-FSR from the pump mode (μ = 0); and a mode-locked Kerr comb (dark soliton) with a 3-FSR spacing is formed with the help of the cascaded process.

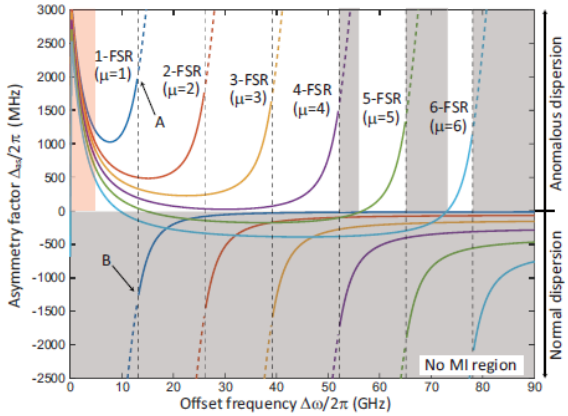

Fig. 2: Theoretical analysis of asymmetry factor versus offset frequency of Aux. mode for each mode.

Figure 3 shows the results of 3-FSR comb generation. Here we used the SiN microring parameters. We set the pump power P_{in} = 500 mW, and the coupling strength $\kappa/(2\pi)$ = 3.34 GHz, the center frequency of mode A at $\omega_0/(2\pi)$ = 191.9 THz, $Q = 7.5\times10^5$, $Q_{ext} = 3.5\times10^6$, $D_1/(2\pi)$ = 378 GHz, and $D_2/(2\pi)$ = −16 MHz for the main mode.

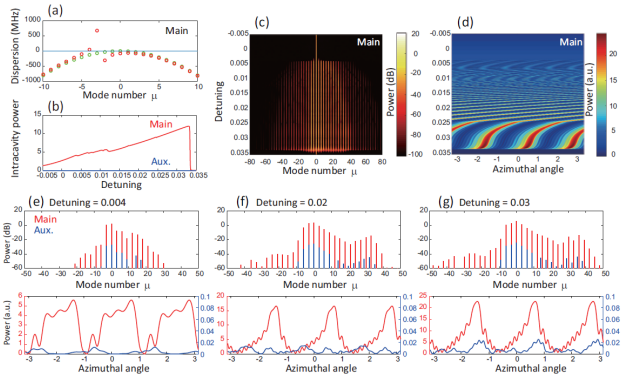

Fig. 3: (a) Cavity dispersion of main mode with mode coupling (red circles) and without mode coupling (green circles). A strong mode interaction occurs with the mode number $\mu = -3$. (b) Average intracavity power and detuning during pump scanning from blue to red. (c,d) Evolution of optical spectrum and time domain waveform versus detuning. (e-g) Simulated optical spectra and temporal waveforms of the main and auxiliary modes with different detunings.

The quality factor, FSR, and dispersion for the auxiliary mode are $Q = 3.7\times10^5$, $D'_1/(2\pi)$ = 391 GHz, and $D'_2/(2\pi)$ = −17 MHz, respectively. The offset frequency is $\Delta\omega/(2\pi)$ = 36 GHz, where the value is determined by the theoretical curve in Fig. 2. Figure 3(a) is the cavity dispersion ($\omega_\mu - \omega_0 - \mu D_1$) of the coupled Main cavity, with (red) and without (green) mode couplings, indicating that a strong mode interaction is present in three modes apart from the pump mode. Figure 3(b-d), respectively, show the average intracavity power, the evolution of the optical spectrum, and the temporal waveform at different normalized pump detunings $t_R(\omega_0-\omega_p)$ (t_R is the roundtrip time of the Main cavity). The initial comb sidebands are generated at 3-FSR, where the strong mode coupling occurred, and then a stable 3-FSR comb is formed without passing through a chaotic state. Even when we set a different initial noise, the trajectory of the intracavity power follows the same path. We had already proven numerically that a deterministic mode-locked dark pulse generation is indeed possible with this scheme, as the authors of Ref. [2,3] claimed in their experimental work.

References

[1] P. Del'Haye, *et al.*, Nature 450, 1214-1217 (2007).

[2] X. Xue, *et al.*, Nat. Photonics 9, 594-600 (2015). G. Lin and Y. K. Chembo, Opt. Lett. 41, 3718–3721 (2016).

[3] X. Xue, *et al.* Laser Photonics Rev. 9, L23-L28 (2015).

[4] Y. K. Chembo, Nanophotonics, 5, 214-230 (2016).

Numerical analysis of optical comb using Lugiato-Lefever equation with stimulated Raman scattering

Atsuhiro Hori (M2)

We conducted a numerical analysis of an optical comb using the Lugiato-Lefever equation and considering stimulated Raman scattering. We revealed that a transverse modes interaction via stimulated Raman scattering is closely related to the quality factor ratio of two transverse modes by comparison with experimental results. Moreover, we studied dark soliton generation via stimulated Raman scattering in a normal dispersion regime, and investigated a new method for dark soliton generation without mode coupling.

Key word : Optical comb, Stimulated Raman scattering, Lugiato-Lefever equation, Dark soliton

1. Introduction

An optical comb is a light source that has an evenly spaced spectrum generated by the Kerr effect or stimulated Raman scattering (SRS), which are nonlinear optical effects in an optical microresonator. Optical combs were first demonstrated in 2007 by T. J. Kippenberg [1]. Since then, the optical comb has been well studied both experimentally and theoretically. In particular, the Lugiato-Lefever equation (LLE) [2] is often used in numerical calculations when theoretical studies are conducted. The LLE is a nonlinear partial differential equation describing the time evolution of an electric field in an optical microresonator derived from a nonlinear Schrödinger equation, which describes the propagation of light in optical fiber and the boundary condition. The LLE cannot be solved analytically, but can be solved numerically by using the Split-Step Fourier Method (SSFM).

In this research, we conducted a numerical analysis on two systems using the LLE with SRS. The first was “Transverse mode interaction via SRS on optical comb generation”. The second was “Dark soliton generation via SRS in normal dispersion regime”.

2. Transverse mode interaction via SRS on optical comb generation

We obtained two experimental results with different spectral shapes depending on the pumping transverse mode as shown Fig. 1.

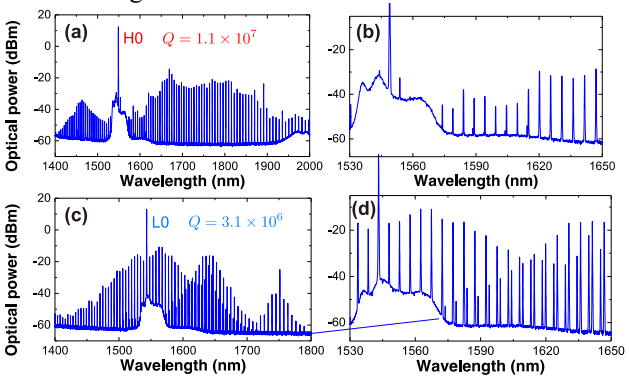

Fig. 1: Optical spectra pumped with different modes.

(a), (b) show spectra obtained with pumping in the high-Q transverse mode and (c), (d) show spectra obtained with pumping in the low-Q transverse mode. In (c) and (d), the comb is generated in a different transverse mode from the pump mode around 1650 nm, which is the center wavelength of the SRS gain.

Using these experimental results as a basis, we conducted a numerical analysis where we noted the quality factor of each transverse mode. The LLE with SRS is described as follows

$$t_R \frac{\partial E(t,\tau)}{\partial t} = \left[-\frac{\alpha_{\mathrm{tot}}}{2} - i\delta_0 + iL\sum_{k=2}^{\infty} \frac{\beta_k}{k!}\left(-i\frac{\partial}{\partial \tau}\right)^k + i(1-f_R)L\gamma|E|^2 \right] E + if_R L\gamma E \int_{-\infty}^{\infty} h_R(\tau')|E(\tau-\tau')|^2 \, d\tau' + \sqrt{\theta}E_{\mathrm{in}}. \quad (1)$$

Here, t and τ represent slow time and fast time, respectively. $t_R, \alpha_{\mathrm{tot}}, \delta_0, L, \beta_k, \gamma, \theta,$ and E_{in} represent round trip time, total cavity loss, detuning, cavity length, kth-order dispersion, nonlinear coefficient, coupled coefficient and input electric field respectively. f_R and h_R are the SRS contribution and the delayed Raman response function. We coupled the LLEs for two transverse modes to allow us to consider transverse mode interaction. Here, we assumed TE_{01} as the pump mode and TE_{00} as the interaction mode with the pump mode. We calculated the effective mode area and dispersion of each mode with the finite element method and used the results for numerical analysis. Fig. 2 shows our simulation results.

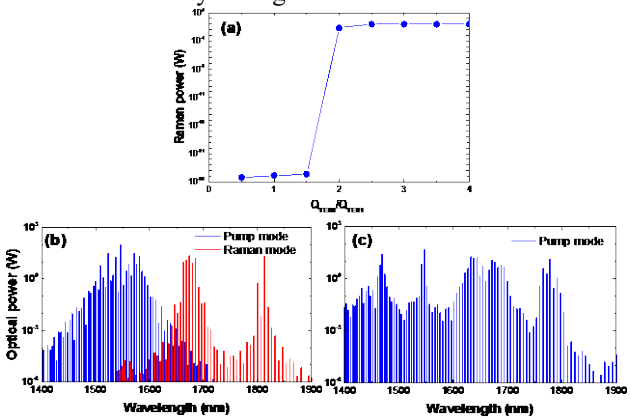

Fig. 2: (a) Intracavity power of TE_{00} versus quality factor ratio between TE_{00} and TE_{01}. (b) Optical spectrum when $Q_{\mathrm{TE}_{00}}/Q_{\mathrm{TE}_{01}} = 3$. (c) Optical spectrum when TE_{00} is pumped.

(a) shows that when $Q_{\mathrm{TE}_{00}}/Q_{\mathrm{TE}_{01}}$ exceeds 2, transverse mode interaction occurs and the intracavity energy transfers from TE_{01} to TE_{00} via SRS. (b) shows the optical spectrum obtained when $Q_{\mathrm{TE}_{00}}/Q_{\mathrm{TE}_{01}} = 3$, which corresponds to our experimental value, and a comb is

generated by SRS in the TE_{00} mode, which is not pumped. On the other hand, when the TE_{00} mode is pumped, the interaction does not occur as shown in (c). These optical spectra agree well with those in Fig. 1.

In summary, we showed that the transverse mode interaction via SRS is closely related to the quality factor of the pump mode, and the interaction occurs only when a low-Q mode is pumped.

3. Dark soliton generation via SRS in normal dispersion regime

In previous studies, dark soliton (DS) generation is demonstrated experimentally using mode coupling [3,4], but those methods are difficult and complicated. Then, we investigated a new method using the LLE for DS generation via SRS.

To conduct a steady analysis, we considered the normalized LLE as follows

$$\frac{\partial u(t,\tau)}{\partial u} = \left(-1 + i\Delta - i\frac{\partial^2}{\partial \tau^2} + i|u|^2 - iT_R'\frac{\partial |u|^2}{\partial \tau}\right)u + S. \qquad (2)$$

where Δ, T_R', and S represent dimensionless values corresponding to detuning, SRS amplitude and input electric field. We assumed the boundary condition $\tau \in [0, L']$, $L' = 20$, $S = 1.6$, and $T_R' = 0.1$, and conducted a steady analysis with detuning Δ as a parameter. Fig. 3 is a bifurcation diagram calculated from equation (2).

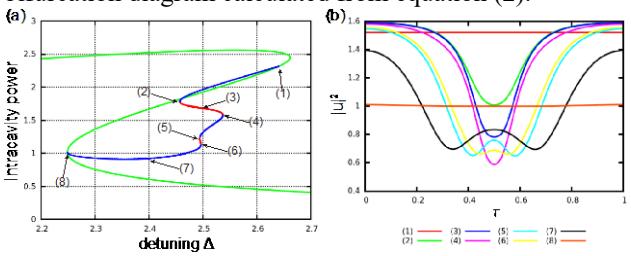

Fig. 3: (a) Bifurcation diagram of equation (2). Green, blue, and red lines show a steady-state solution of homogeneous light, unstable DS and stable DS respectively. (b) Time waveform at each equilibrium point.

(a) indicates that stable DS solutions exist even when SRS is considered. DS solutions exist in the inside of bistability of a homogenous solution, and have some saddle-node bifurcations. (b) shows that the DS solutions connect with two homogeneous solutions, with the peak power and pulse width varying gradually. Then, we investigated the stability of a stable DS solution for different T_R' values . Stable DS solutions remain stable in the $0 \leq T_R' < 2.01122 \times 10^{-2}$ range , but become unstable in the $T_R' \geq 2.01122 \times 10^{-2}$ range . Moreover, the position of the saddle-node bifurcation points at both ends of a stable DS solution remain unchanged in the stable range.

To investigate a method for realizing stable DS solutions with CW pumping, we conducted a numerical analysis using parameters converted from the dimensionless values used in the calculation used for Fig.3. First, we swept the detuning δ_0 from 0 to 1.582×10^{-3}, which corresponds to stable DS solutions, but the time waveform remained CW light. This result showed that SRS does not occur with the parameters of an existing stable DS solution, and so DS generation is impossible solely by sweeping the detuning. Therefore, first, we set a high pump power and performed the sweeping detuning to generate the Raman comb, and then set the pump power at the initial value as shown in Fig. 4.

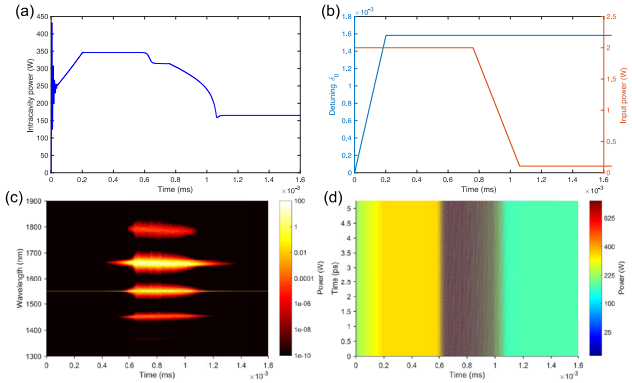

Fig. 4: (a) Intracavity power versus time *t*. (b) Detuning and input power. (c,d) Evolution of spectrum and time waveform.

(c) shows that a sweeping detuned Raman comb is generated around 1650 nm, then other combs are generated via anti-Stokes SRS, cascaded SRS, and four-wave mixing. We expected that from this state, only a single comb around pump will remain by decreasing the pump power, but (c) indicates that all the combs disappeared. In addition to this method, we tried another method where the detuning was first swept from 0 to 3.0×10^{-3}, and then the pump power was decreased to the initial detuning sweeping value of 1.582×10^{-3}, but all the combs disappeared as in Fig. 4.

In this research, we were unable to discover a new method for DS generation, but more detailed analysis may provide a clue. Our analysis considered only a homogeneous solution. A DS solution and a route to a stable DS solution remains obscure, and so we think that the next task is to undertake an analysis with regard to a periodic solution.

References

[1] Del'Haye, P., Schliesser, A., Arcizet, O., Wilken, T., Holzwarth, R. & Kippenberg, T. J., Nature **450,** 1214–1217 (2007).

[2] Lugiato, L. & Lefever, R., Physical Review Letters **58,** 2209–2211 (1987).

[3] Xue, X., Xuan, Y., Liu, Y., Wang, P. H., Chen, S., Wang, J., Leaird, D. E., Qi, M. & Weiner, A. M., Nature Photonics **9,** 594–600 (2015).

[4] Xue, X., Xuan, Y., Wang, P. H., Liu, Y., Leaird, D. E., Qi, M. & Weiner, A. M., Laser & Photonics Reviews **9,** L23–L28 (2015).

Control of four wave mixing by using high-order dispersion in silica toroid microcavities

Minori Hasegawa (B4)

By using high-Q microcavities, we can efficiently generate non-linear photonic effects using only a continuous wave and a low-power laser as a pump. It has been reported that one non-linear effect, namely four wave mixing (FWM), requires anomalous dispersion. However, recent studies have revealed that FWM can occur with normal dispersion under special conditions. This study suggests a dispersion control technique for controlling normal dispersion FWM by using high-order dispersion.

Key words: Microresonator, microcomb, four-wave mixing

1. Background

Whispering-gallery mode (WGM) cavities have a full-reflection construction designed to confine light in a very small space. In WGM cavities, the light density increases, and there is a strong interaction between light and material. Therefore, the threshold of the non-linear effects is low. This means WGM cavities are suitable for the generation of non-linear effects.

Various non-linear effects can occur in WGM cavities including four wave mixing (FWM) and third harmonic generation (THG). FWM is not a phenomenon that occurs only in WGM cavities. When FWM occurs in WGM cavities, there is a limitation, which means that no other light can exist without being in a resonance mode. FWM in WGM cavities presents a comb-like spectrum that has an evenly-spaced vertical mode. This spectrum is called a photonic Kerr comb because it requires a balance between anomalous dispersion and photonic Kerr effects.

THG is a phenomenon that converts to a light with a triple frequency. THG is an effective approach for visible light emission when the pump wavelength is near 1550 nm. THG requires a phase matching condition. Due to the effects of dispersion, the same horizontal mode does not definitely satisfy the phase matching condition. A high-order mode possibly satisfies the condition.

2. Calculation

In recent studies, FWM has been observed under normal dispersion conditions by using high-order dispersion. FWM in a normal dispersion has a feature that appears far from the pump wave in a narrow band. This may offer a new approach to wavelength conversion.

We use the finite element method for the calculation. It can calculate the resonance frequency from the refractive index, and a Sellmeier equation can calculate the refractive index from the resonance frequency. By using this calculation cycle, we can calculate both structure dispersion and material dispersion.

We choose silica toroid microcavities, which have two parameters, the major radius and the minor radius, and this is advantageous for dispersion calculation.

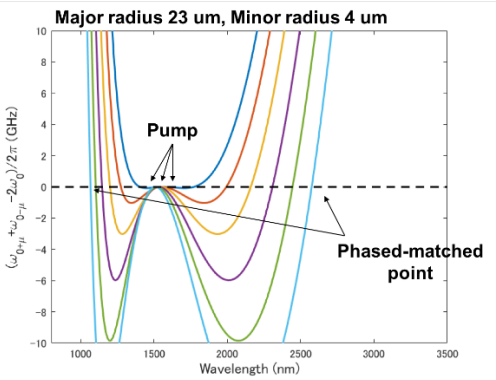

Figure 1 : Phase matching condition of FWM in a cavity（M=23 μm, m=4 μm）

The horizontal axis is pump wavelength and the vertical axis is phase mismatch. When the pump wavelength becomes shorter, the idler light wavelength also becomes shorter.

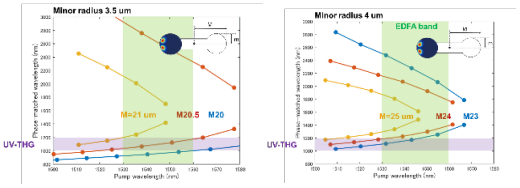

Figure 2 : (a)(b) Comparison m=3.5 μm and m=4 μm, both figures show the relationship between pump wavelength and FWM.

Figure 3 suggests the possibility of ultra-violet (UV) light generation because the idler light is shorter than 1200 nm. UV generation via THG is unrealistic, because large cavities are difficult to fabricate.

3. Experiment

We used silica toroid microcavities in this study. We made a silicon post by using XeF_2 etching, and laser reflow. Size control was very difficult, especially when we employed laser reflow. Size control is dependent on lasing power and time. The laser output was controlled simply with a knob, which requires experience to operate. We made cavities with a high 10^7-order Q.

In this study, to generate FWM, for the pump we used a CW laser whose power was amplified with an erbium-doped fiber amplifier. We used tapered fiber to

inject light into cavities, which was made by stretching heated optical fiber. When the tapered fiber is near the cavities (100～200 nm), an evanescent wave penetrates the cavities. We moved the tapered fiber by operating an electric stage.

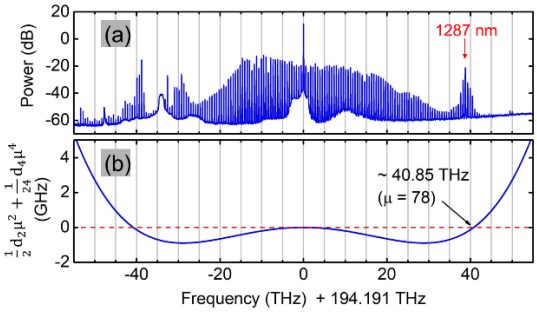

Figure 3: (a) Recorded FWM spectra with a microcavity having major radius M=60 μm and minor radius m=4.5μm. (b) Calculated dispersion by using FEM.

Figure 3 shows the dispersion design of a silica toroid microcavity realized by using high-order dispersion similar to the calculation

4. Conclusions and future tasks

In this study, we successfully controlled normal dispersion FWM by using high-order dispersion. This way of designing dispersion must form the basis of a future study into the generation of non-linear photonic effects.

We discovered new tasks that we must undertake to improve the accuracy with which microcavities are fabricated. The etching and reflow process is currently less than perfect

References

[1] A. Yariv, Quantum Electronics, 3rd ed. (John Wiley & Sons, 1989).
[2] T. W. Hansch, “Nobel Lecture: Passion for precision”, Rev. Mod. Phys. 78, 1297 (2005).
[3] K. J. Vahala, “Optical microcavities,” Nature **424**, 839 (2003).
[4] P. Del’Haye, A. Schliesser, O. Arcizet, T. Wilken, R. Holzwarth, and T. J. Kippenberg, “Optical frequency comb generation from a monolithic microresonator,” Nature **450**, 1214 (2007).

#Note added by Takasumi Tanabe. If you find any difficulties with contents and language, please contact me.

Statistical Data

Publications (Apr. 2017 – Mar. 2018)

Journal papers

[1] S. Fujii, T. Kato, R. Suzuki, and T. Tanabe, “Third-harmonic blue light generation from Kerr clustered combs and dispersive waves,” Opt. Lett., Vol. 42, No. 10, pp. 2010-2013 (2017).

[2] Y. Mizumoto, H. Kangawa, H. Itobe, T. Tanabe, and Y. Kakinuma, “Influence of crystal anisotropy on subsurface damage in ultra-precision cylindrical turning of CaF_2,” Precis. Eng., Vol. 49, pp. 104-114 (2017).

[3] N. A. B. Daud, Y. Ooka, T. Tabata, T. Tetsumoto, and T. Tanabe, “Electro-optic modulator based on photolithography fabricated p-i-n integrated photonic crystal nanocavity,” IEICE Transactions on Electronics, Vol. E100-C, No.8, pp.670-674 (2017).

[4] W. Yoshiki, Y. Honda, T. Tetsumoto, K. Furusawa, N. Sekine, and T. Tanabe, “All-optical tunable buffering with coupled ultra-high Qwhispering gallery mode microcavities,” Sci. Rep. 7, 28758 (2017).

[5] T. Tetsumoto, H. Kumazaki, K. Furusawa, N. Sekine, and T. Tanabe, “Design, fabrication and characterization of a high Q silica nanobeam cavity with orthogonal resonant modes,” IEEE Photon. J. Vol. 9, No. 5, 4502609 (9 pages) (2017).

[6] R. Suzuki, T. Kato, T. Kobatake, and T. Tanabe, “Suppression of optomechanical parametric oscillation in a toroid microcavity assisted by a Kerr comb,” Opt. Express, Vol. 25, No. 23, pp. 28806-28816 (2017).

[7] S. Fujii, A. Hori,T. Kato, R. Suzuki, Y. Okabe, W. Yoshiki, A. C.-Jinnai, and T. Tanabe, “Effect on Kerr comb generation in a clockwise and counter-clockwise mode coupled microcavity,” Opt. Express, Vol. 25, No. 23, pp. 28969-28982 (2017). [arXiv:1709.10226v1]

[8] S. Fujii, T. Kato, R. Suzuki, A. Hori, and T. Tanabe, “Transition between Kerr comb and stimulated Raman comb in a silica whispering gallery mode microcavity,” J. Opt. Soc. Amer. B, Vol. 35, No. 1, pp. 100-106 (2018). (Editor’s pick) [arXiv:1712.04601v1]

International conferences

[1] Y. Honda, W. Yoshiki, T. Tetsumoto, S. Fujii, K. Furusawa, N. Sekine, and T. Tanabe, “Tuning supermode splitting for stimulated Brillouin scattering,” The 6th Advances Lasers and Photon Sources Conference (ALPS’17), ALPS8-4, Yokohama, April 18-21 (2017).

[2] N. Hirota, W. Yoshiki, A. Hori, K. Namiki, K. Sato, H. Maki, and T. Tanabe, “Growing carbon nanotubes on a silica toroid microcavity to observe saturable absorption,” The 6th Advances Lasers and Photon Sources Conference (ALPS’17), ALPS11-3, Yokohama, April 18-21 (2017).

[3] S. Fujii, T. Kato, A. Chen-Jinnai, R. Suzuki, and T. Tanabe, “Broad bandwidth visible light generation via third-order nonlinear interaction in silica toroid microcavity,” The 6th Advances Lasers and Photon Sources Conference (ALPS’17), ALPSp14-03, Yokohama, April 18-21 (2017).

[4] N. A. B. Daud, Y. Ooka, T. Tetsumoto, and T. Tanabe, “Photonic crystal nanocavity photodetector integrated with p-i-n junction fabricated by photolithography process,” International Conference on Nano-photonics and Nano-optoelectronics (ICNN2017), ICNN8-3, Yokohama, April 18-21 (2017).

[5] T. Tetsumoto, Y. Ooka, N. A. B. Daud, N. Kamioka, T. Okamura, and T. Tanabe, “A CMOS compatible in-plane compact wavelength demultiplexer based on photonic crystal nanocavities,” International Conference on Nano-photonics and Nano-optoelectronics (ICNN2017), ICNN2-5, Yokohama, April 18-21 (2017).

[6] W. Yoshiki, Y. Honda, M. Kobayashi, T. Tetsumoto, and T. Tanabe, “Adiabatic frequency conversion in an ultra-high-Q silica microcavity using the Kerr effect,” CLEO:2017, SM2N1, San Jose, May 14-19 (2017).

[7] W. Yoshiki, Y. Honda, T. Tetsumoto, K. Furusawa, N. Sekine, and T. Tanabe, “Demonstration of all-optical tunable buffering using coupled ultra-high-Q silica toroid microcavities,” CLEO:2017, SM2N2, San Jose, May 14-19 (2017).

[8] T. Tetsumoto, H. Kumazaki, K. Furusawa, N. Sekine, A. Kasamatsu, and T. Tanabe, “High Q silica nanobeam cavity for simultaneous resonance of TE- and TM-like modes,” CLEO:2017, JW2A, San Jose, May 14-19 (2017).

[9] A. Kubota, R. Suzuki, S. Fujii, and T. Tanabe, “Third-harmonic generation with Kerr frequency comb in silica rod microcavity,” Conference on Lasers and Electro-Optics – European Quantum Electronics Conference (CLEO/Europe – EQEC 2017), CK-2.5, Munich, 25-29 June (2017)

[10] M. Fuchida, H. Itobe, R. Suzuki, Y. Nakagawa, W. Yoshiki, Y. Mizumoto, Y. Kakinuma, S. Okuda, H. Sasada, and T. Tanabe, “Dispersion tailoring of a crystalline whispering gallery mode microcavity for optical Kerr frequency comb generation,” Conference on Lasers and Electro-Optics – European Quantum Electronics Conference (CLEO/Europe – EQEC 2017), CK-5.3, Munich, 25-29 June (2017).

[11] Y. Honda, W. Yoshiki, T. Tetsumoto, S. Fujii, K. Furusawa, N. Sekine, and T. Tanabe, “Brillouin lasing in coupled silica toroid microcavities,” Conference on Lasers and Electro-Optics – European Quantum Electronics Conference (CLEO/Europe – EQEC 2017), CD-5.1, Munich, 25-29 June (2017).

[12] R. Suzuki, T. Kato, T. Kobatake, and T. Tanabe, “Cavity optomechanical coupling to multiple resonances assisted by Kerr comb generation in toroid microcavity,” Conference on Lasers and Electro-Optics – European Quantum Electronics Conference (CLEO/Europe – EQEC 2017), CD-P.7, Munich, 25-29 June (2017).

[13] A. Hori, T. Kato, R. Suzuki, S. Fujii, T. Kobatake, and T. Tanabe, “Interaction of transverse modes via stimulated Raman scattering on comb generation in a silica toroid Microcavity,” Conference on Lasers and Electro-Optics – European Quantum Electronics Conference (CLEO/Europe – EQEC 2017), CD-P.25, Munich, 25-29 June (2017).

[14] T. Tanabe, “Stimulated Raman scattering comb in a silica microcavity,” Integrated Photonics

Research, Silicon, and Nano-Photonics (IPR 2017), IM4A.3, New Orleans, 24-27 July (2017). (invited)

[15] T. Tetsumoto, H. Kumazaki, Y. Honda, and T. Tanabe, "Demonstration of direct coupling between a toroid microcavity and a photonic crystal waveguide," The Pacific Rim Conference on Lasers and Electro-Optics (CLEO-Pacific Rim 2017), 2-1L-4, Singapore, 31 July – 4 August (2017).

[16] N. A. B. Daud, Y. Ooka, T. Tetsumoto, and T. Tanabe, "SiO2 clad active and passive photonic crystal nanocavity devices fabricated with photolithography," The Pacific Rim Conference on Lasers and Electro-Optics (CLEO-Pacific Rim 2017), P3‐119, Singapore, 31 July – 4 August (2017).

[17] S. Fujii, Y. Okabe, T. Kato, R. Suzuki, Y. Honda, A. Hori, and T. Tanabe, "Numerical simulation of dark soliton generation in coupled microcavity system," The 24th Congress of the International Commissions for Optics (ICO-24), M1E-07, Tokyo, 21-25 August (2017).

[18] T. Tetsumoto, H. Kumazaki, Y. Honda, W. Yoshiki, K. Furusawa, N. Sekine, and T. Tanabe, "Experimental investigation of feasability of a hybrid system of a photonic crystal waveguide & a toroidal microcavity," The 24th Congress of the International Commissions for Optics (ICO-24), F1E-06, Tokyo, 21-25 August (2017).

[19] S. Fujii, Y. Okabe, T. Kato, R. Suzuki, A. Hori, and T. Tanabe, "Nonlinear coupled mode equations for Kerr comb generation in coupled microcavity system," Frontiers in Optics/Laser Science Conference (FiO/LS), FTu2D.3, Washington DC, September 17-21 (2017).

[20] T. Tetsumoto, H. Kumazaki, K. Furusawa, N. Sekine, and T. Tanabe, "Investigation of an optimal coupling condition with a nanobeam cavity made of low refractive index material," Frontiers in Optics/Laser Science Conference (FiO/LS), FTu2D.3, Washington DC, September 17-21 (2017)

[21] T. Okamura, M. Kobayashi, S. Fujii, and T. Tanabe, "Highly sensitive ammonia gas detection with a silica toroid microcavity packaged in a box," Frontiers in Optics/Laser Science Conference (FiO/LS), FTu2D.3, Washington DC, September 17-21 (2017).

[22] R. Suzuki, A. Kubota, S. Fujii, A. Hori, T. Kato, and T. Tanabe, "Raman Comb Formation in Silica Rod Microresonator," Frontiers in Optics/Laser Science Conference (FiO/LS), JW3A.76, Washington DC, September 17-21 (2017).

[23] N. Kamioka, T. Tetsumoto, and T. Tanabe, "FDTD with an off-diagonal permittivity tensor component to study the magneto-optical effect in a slow light waveguide," Frontiers in Optics/Laser Science Conference (FiO/LS), JW4A.50, Washington DC, September 17-21 (2017).

[24] T. Tanabe, Y. Ooka, N. A. B. Daud, and T. Tetsumoto, "Robust CMOS compatible photonic crystal nanocavity and DEMUX filter," Asia Communications and Photonics Conference (ACP 2017), M1F.1, Guangzhou, November 10-13 (2017). (invited)

[25] T. Tetsumoto, H. Kumazaki, R. Ishida, and T. Tanabe, "Investigation of the influence of proximity effect and randomness on photolithographically fabricated photonic crystal nanobeam cavity," SPIE NanoPhotonics Australia 2017, 10456-63, Melbourne, December 10-13 (2017). [Proc. SPIE, Vol. 10456, 104561Y (2018).]

[26] T. Kumagai, N. Hirota, K. Sato, K. Namiki, A. Hori, H. Maki, and T. Tanabe, “Saturable absorption by carbon nanotubes on silica microtoroids for stable mode locking,” SPIE Photonics West 2018, 10518-16, San Francisco, January 27-February 1 (2018). [Proc. SPIE, Vol. 10518, 105180H (2018).]

Awards

May 2017 Shun Fujii, “The 6th Advanced Lasers and Photon Sources, Best Student Award”

September 2017 Shun Fujii, “Milton Chang & Incubic student travel grant”

Dissertations

PhD thesis:

Tomohiro Tetsumoto, "Tailoring optical resonances in photonic crystals with an optical nanofiber," Feb. 2018.

Master thesis:

Naoya Hirota "Saturable absorption and growth of carbon nanotubes on silica toroid microcavity by chemical vapor deposition"

Shun Fujii "Study on nonlinear optical effects and mode coupling in high-Q optical microcavities"

Atsuhiro Hori "Theoretical analysis of optical comb based on Lugiato-Lefever equations with stimulated Raman scattering"

Bachelor thesis:

Rammaru Ishida "Optical measurement of MoS2 for application with photonic nanostructures"

Shengi Jin "Optimization of photonic crystal DeMUX fabricated with phtolithography"

Minori Hasegawa "Control of four-wave mixing by high-order dispersion engineering in silica toroid microresonator"

Seminars

Date: August 22, 2017 16:30-17:40
Speaker: Dr. Yoshitomo Okawachi, Columbia University
Title: Frequency comb in microcavity and professional development opportunity in OSA

Date: August 22, 2017 17:45-18:15
Speaker: Prof. Sun Changzheng, Tsinghua National Laborator
Title: AlN microring based Raman lasers and Kerr combs

Date: October 10, 2017 14:45-16:15
Speaker: Prof. Jonathan Finley (Technische Universität München, Germany)
Title: Quantum optics with semiconductor artificial atoms

Date: October 17, 2017 16:30-18:00
Speaker: Kyoko Kitamura (Kyoto Institute of Technology)
Title: Beam shaping, polarization, phase and direction control using a single semiconductor laser (in Japanese)

Date: November 8, 2017 16:30-18:00
Speaker: Dr. Fuchuan Lei (OIST, Japan)
Title: Laser dynamics and its application on mode control in Whispering gallery microcavities

KEIO-TUM workshop on SOLID-STATE NANOSCIENCE

Date: June 30, 2017　10:00-16:00
Place: ZNN room 1.003, Walter Schott Institute, Technische Universität München, Germany

10:15–10:45 Jon Finley, “Semiconductor-based spin quantum memories”
10:45–11:00 Michael Kaniber, “Linear and non-linear optical properties of atomicall-thin semiconductors”
11:00–11:15 Jochen Bissinger, “GaAs-AlGaAs core-shell nanowire lasers on silicon”
(11:15–12:45 lunch at “Garchinger Augustiner”)
12:45–13:15 Takasumi Tanabe, “Signal processing with photonic crystal and WGM microcavities”
13:15–13:30 Shun Fujii, “Frequency comb generation in WGM microcavity: The effect of SRS and THG”
13:30–13:45 Yoshihiro Honda, “Stimulated Brillioun Scattering Lasing in coupled WGM microcavity system”
(13:45–14:15 coffee break)
14:15–14:45 Martin Brandt, “Electrical Readout of NV- centers in diamond”
14:45–15:00 Lukas Stelzer, “Broadband electrically detected magnetic resonance using optimal control”
15:00–15:15 David Franke, “Mechanical tuning of donor nuclear spins in silicon”